Pushing the limits of atomistic simulations towards ultra-high temperature: a machine-learning force field for ZrB_2

Yanhui Zhang, Alessandro Lunghi, Stefano Sanvito[1]
School of Physics and CRANN, Trinity College, Dublin 2, Dublin, Ireland

Determining thermal and physical quantities across a broad temperature domain, especially up to the ultra-high temperature region, is a formidable theoretical and experimental challenge. At the same time it is essential for understanding the performance of ultra-high temperature ceramic (UHTC) materials. Here we present the development of a machine-learning force field for ZrB_2, one of the primary members of the UHTC family with a complex bonding structure. The force field exhibits chemistry accuracy for both energies and forces and can reproduce structural, elastic and phonon properties, including thermal expansion and thermal transport. A thorough comparison with available empirical potentials shows that our force field outperforms the competitors. Most importantly, its effectiveness is extended from room temperature to the ultra-high temperature region (up to ∼2,500 K), where measurements are very difficult, costly and some time impossible. Our work demonstrates that machine-learning force fields can be used for simulations of materials in a harsh environment, where no experimental tools are available, but crucial for a number of engineering applications, such as in aerospace, aviation and nuclear.

I. INTRODUCTION

Transition metal borides, carbides and nitrides, such as ZrB_2, HfB_2, ZrC and TiN, are formed by combining a light element from group III, IV or V, with a refractory transition metal. They are generally characterized by an unusual combination of physical and chemical properties, such as an extremely high melting temperature ($T > 3000$ °C), great hardness, and both good chemical stability and mechanical strength at high temperatures[1]. These compounds are usually referred to as ultra-high-temperature ceramics (UHTCs). They are considered to be the most relevant materials set for high-temperature applications in the aerospace (e.g. thermal protection systems for hypersonic or atmospheric reusable re-entry vehicles, propulsion components, combustion chambers, engine intakes or rocket nozzles), energy (e.g. nuclear fission and fusion, energy harvesting, concentrated solar power) and high-technology (e.g. high temperature electrodes, high speed machining tools, molten metal containment) sectors.[2–5]

UHTCs containing either ZrB_2 or HfB_2 are possibly the most widely studied members of this class due to their additional resistance to oxidation observed up to 2000 °C. In particular, they hold expectations as a replacement of silicon-based compounds, such as SiC, Si_3N_4 and $MoSi_2$, whose operation range is limited to approximately 1700 °C. Notably, the hot section of aerospace and nuclear facilities can easily approach working temperatures of 2000 °C in a very short time (0.1 second to a couple of minutes), meaning that the typical thermal shocks are considerable. Clearly, the knowledge and control of the thermal and physical properties with temperature is crucial for optimizing and understanding the performances of these engineering materials over their entire operation range.

Ideally, it would be important to study these materials' properties in the conditions found in their service environment[6]. This is particularly relevant for temperature effects, since the knowledge of T-dependent properties allows one to accurately assess the impact of thermal shock, creep and fatigue, and to understand the sensitivity of the possible engineering components to thermal-stress-induced failures. Unfortunately, the experimental characterization of high-temperature properties is very challenging and costly, if not impossible[7], so that only an incomplete picture is captured in most cases. This means that the engineering design is somehow blind to the most extreme part of the operation conditions. All these difficulties make theoretical simulations a really valuable toolset to study the material's responses to such extreme conditions. Unfortunately, a universally accurate and efficient simulation method is still not available.

Ab-initio molecular dynamics can manage high temperatures in a natural fashion, but its high computational cost makes it practical for the simulation of only a few hundred atoms for up to hundreds of picoseconds. This is usually not sufficient, since the required simulation scale needed to solve many problems of interest goes far beyond thousands of atoms and several thousands of nanoseconds or even microseconds. In contrast, empirical force fields can extend to the desired time and length scales. These are computationally efficient due to the analytical functions employed to express the total energy and the forces. However, they usually struggle to handle several features specific to the high-temperature domain, namely i) the large variation of physical properties across a broad temperature range; ii) the reliability of the extrapolated data from empirical parameters; iii) the strong anharmonic effects taking place at ultra-high temperature, especially close to the melting point ($T_m \sim 3000$°C for UHTCs).

A promising solution to this conundrum is to use machine-learning force fields (MLFFs). They can reach quantum-chemistry accuracy at a computational cost comparable with that of conventional effective potentials. The formulation and implementation of MLFFs are rapidly becoming an active research area, and the latest generation of MLFF has also a great potential for the investigation of molecules and solids[8], of amorphous phases[9] and of multi-component materials[10,11].

In this work we take the spectral neighbor analysis potential (SNAP) formulation[12] to derive a robust MLFF for ZrB_2, a prototypical UHTC material. ZrB_2 has the AlB_2 structure ($P6_3/mmc$) with a nano-laminate stacking of B and Zr layers. The B layer has a 2D graphene-like structure with strong covalent bonds, while the Zr-layer is dominated by metallic bonding. In addition, the Zr-B interaction has a mixed covalent and ionic nature[13]. Previous attempts to construct atomic potentials for ZrB_2 include Tersoff potentials[14] and reactive force-fields (ReaxFF)[15]. These, however, struggle with the T-dependent thermo-physical properties. For instance, they run into problems when calculating the thermal conductivity at 1000 K[16] and they are not accurate in describ-

ing room-temperature elasticity. These difficulties are attributed to the inability to simultaneously describe: i) the rather chemically different constituent elements, ii) the complex bonding nature comprising a mixture of metallic, covalent and ionic interactions, iii) the intricate response to a wide range of heat and mechanical loads.

By tuning the SNAP parameters from a rich variety of reference configurations, our derived MLFF demonstrates a surprisingly accurate ability to face the aforementioned challenges. A brief description of the SNAP formalism, the training datasets and the procedure to determine the model parameters is presented in the following section. Thereafter we apply the developed MLFF to predict the fundamental physical properties of ZrB_2. The results are compared with available experimental and simulation findings. Our SNAP potential exhibits robustness in reproducing the T-dependent physical properties and a good transferability across a wide range of temperatures and deformations. This work provides a framework to study the high-temperature behavior of materials and it paves the way for accurate atomistic simulations of UHTCs.

II. CONSTRUCTION OF THE FORCE FIELD

A. The SNAP model

The model employed in this work is the many-body SNAP force field[8,12], whose main features are briefly outlined here. In general we can write the total energy as

$$E_{\rm total}(\vec{r}^N) = E_{\rm ZBL}(\vec{r}^N) + E_{\rm SNAP}(\vec{r}^N)\,, \qquad (1)$$

where $\vec{r}^N$ is the configuration vector containing the N atomic positions. The Ziegler-Biersack-Littmark (ZBL)[17] empirical potential, $E_{\rm ZBL}(\vec{r}^N)$, is introduced to provide a repulsive short-range interaction, while $E_{\rm SNAP}$ captures the effects arising from the local atomic environments. SNAP assumes that the energy of a collection of atoms can be decomposed into separate atomic contributions, $E^i_{\rm SNAP}$. The energy associated to the i-th atom, $E^i_{\rm SNAP}$, then depends on the local atomic environment, which is described by using the bispectrum components[18] ($\vec{B}^i$= B^i_1, ...,B^i_K). Thus the SNAP potential writes as a linear combination of $\vec{B}^i$, namely as

$$E_{\rm SNAP} = \sum_{i=1}^{N} E^i_{\rm SNAP}(\vec{B}^i) = \sum_{i=1}^{N}\{\beta_0^{\alpha_i} + \sum_{k=1}^{K}\beta_k^{\alpha_i}B^i_k\}\,. \quad (2)$$

Here α_i describes the chemical identity of atom i, while β^α_k are the coefficients of expansion for the atoms of type α. K is the number of bispectrum components used to describe the local atomic environment. This is related to the maximum angular momentum taken in the definition of the hyper-spherical harmonics expansion (see next paragraph).

In practice SNAP knows about the local atomic environment of each atom by projecting the local neighbour density within a radial cutoff, $R_{\rm cut}$, onto a basis of hyperspherical harmonics in four dimensions. This choice of representation for the atomic positions is invariant under rotation, atomic permutation and translation. The details of how the B^i_k are calculated are provided in reference[18]. In general, specifying small values for $R_{\rm cut}$ and K produces a coarse description of the local atomic environment. In contrast, large values will enable one to resolve fine structural differences. The coefficients β^α_k are optimized to reproduce the energies of a large set of configurations computed with density functional theory (DFT). The training process is performed by minimizing the penalty function,

$$\Delta E = |\omega \cdot E_{\rm FF} - E_{\rm DFT}|^2 + \lambda|\beta|^2\,, \qquad (3)$$

where $E_{\rm FF}$ and $E_{\rm DFT}$ are, respectively, the energy predicted by Eq. (1) and the corresponding DFT reference. The second term of Eq. (3) penalizes large β^α_k values in order to avoid over-fitting problems, with λ controlling this regularization process. The weight of the parameter ω is designed to control the relative relevance of different configurations. In this work, all configurations are set equivalent, so that ω=1. Detailed convergence tests for λ, K and $R_{\rm cut}$, are shown in Fig. S1 of the supplementary information (SI). Their final values, together with the ZBL potential parameters are summarized in Table I.

TABLE I. SNAP and ZBL potential parameters used for our optimized ZrB_2 force field. λ is the regularization parameter; K the number of bispectrum components; $R_{\rm cut}$ the cutoff radius of the neighbor density function; $R_{zbl,i}$ and $R_{zbl,o}$ the inner and outer cutoff of the switching function for ramping the energies, forces and curvatures smoothly to zero; $Z_{\rm Zr}$ and $Z_{\rm B}$ the atomic number of the Zr and B atoms.

Potential	Parameter	Value
SNAP	λ	0
SNAP	K	55
SNAP	$R_{\rm cut}$	4.5 Å
ZBL	$R_{zbl,i}$	4.0 Å
ZBL	$R_{zbl,o}$	4.8 Å
ZBL	$Z_{\rm Zr}$	40
ZBL	$Z_{\rm B}$	5

B. DFT datasets

A pool of diverse atomic configurations needs to be included in the DFT reference dataset in order to represent the widest variety of local atomic environments. Such diversity is critical for the construction of a robust force field able to fully capture the features of the potential energy surface. Our training dataset comprises a total of approximately 150,000 local atomic environments extracted from 1850 configurations, while the test dataset contains around 137,000 local atomic environments. Those configurations include randomly distorted supercells (1109), deformed cells (1033), molecular-dynamics snapshots (1457), etc. A detailed description of our DFT dataset and its generation scheme is tabulated in Table II. Notably different classes of data sample different regions of the potential energy surface. In particular each class is designed to target at a variety of properties in the following way (see Table II for the details of each class):

- *EOS I/II* map the elasticity and the general profile of the potential energy surface;

- *Distorted I/II* capture the phonon band-structure and the thermal conductivity;
- *Deformed I/II/III* describe the T-dependent elasticity, thermal expansion and anharmonicity at high temperature;
- *MD snapshots I/II* ensure the dynamic stability of the crystalline structure.

The energies and the atomic forces, as calculated from DFT for the aforementioned dataset, are all collected. The SNAP force field for ZrB_2 is then trained on the energies of the data classes: *EOS I*, *Distorted I&II*, *Deformed I* and *MD snapshots I*, while *EOS I*, *Deformed II & III* and *MD snapshots II* are used for testing and validation purposes. The diversity of our training and test sets is further illustrated by the dimension reduction analysis presented in Fig. S2 of the SI, while their energy distribution is presented in Fig. S3.

C. Computational details

All DFT calculations are performed using the plane-wave basis projector augmented wave method[19] as implemented in the VASP code[20]. The generalized gradient approximation of the exchange and correlation functional with the Perdew-Burke-Ernzerhof (PBE) parametrization[21] is used throughout. In addition, the damped van der Waals correction, DFT-D2, is included to approximate dispersive interactions[22]. The reliability of the PBE+D2 method in describing transition metal diborides has been validated already in reference[23]. The Brillouin zone is sampled by using the Monkhorst-Pack method with a k-point spacing of 0.02 $Å^{-1}$. The kinetic energy cutoff of the plane waves is set to 500 eV. Those parameters have been tested to ensure an energy convergence of 1 meV/atom.

All molecular dynamic (MD) simulations are performed with the LAMMPS package[24] with a time step of 1 fs. The damping parameters for the temperature and pressure are 100 and 800 fs, respectively. The calculations of the thermal expansion, thermal conductivity and elastic moduli are carried out using $6 \times 6 \times 6$ supercells. More details on the MD simulations can be found in the SI.

D. Accuracy of SNAP force field

The SNAP-predicted energies (in unit of eV/atom) and atomic forces (in unit of eV/Å) compare extremely well to their DFT references. The linear regression analysis of energies in Fig. 1(a) gives the angular coefficients of 1.0004 and 1.0006 for the training and test sets, respectively. Being so close to 1 demonstrates that the quality of the SNAP energies is almost the same as that of DFT, regardless on whether the configurations were included or not in the training process. At the same time [see Fig. 1(b)] the linear regression coefficients computed over the training (test) set for the atomic forces along the x, y and z directions are 0.9878 (0.9643), 0.9869 (0.9611) and 1.0099 (0.9932), respectively. This quality translates in a root mean squared error (RMS) over the energy of 1.3 meV/atom and 4.7 meV/atom, respectively for the training and test set. The RMS for the atomic forces is 25 meV/Å (45 meV/Å) for the training (test) set. In order to put these results in prospective, a recent high-quality gaussian approximation potential for carbon-based materials has achieved a RMS of 28 meV/Å and 270 meV/Å over the in-plane forces of graphene and amorphous carbon, respectively[25]. As such, our generated SNAP appears to yield a near to quantum-chemistry accuracy and it is fully competitive with other advanced force field classes.

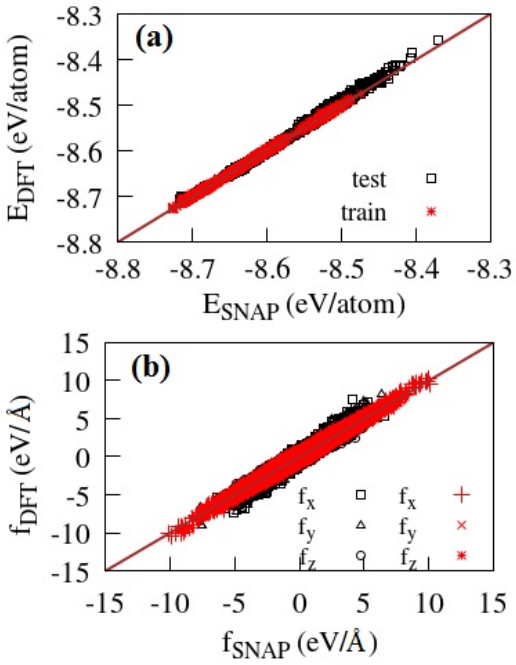

FIG. 1. (color online) SNAP predictions against the DFT references for (a) the energies (eV/atom) and (b) the atomic forces (eV/Å). The training (test) set contains 1850 (1752) configurations, with roughly 449,000 (411,000) force data. Note that the forces were not explicitly included in the training.

Furthermore, the SNAP force field demonstrates an excellent performance on describing the energy landscape against the variation of structural parameters as shown in Fig. 2. In this case the target property is the dependence of the total energy over the lattice parameters, a and c, which are changed with respect to their equilibrium values. The DFT references for this test are contained in *EOS II* dataset, which is not used for the training. Note, in fact, that the largest lattice strain included in the training set is of only 1.3% (*EOS I* dataset, see the corresponding region marked using the grey box in Fig. 2). In Fig. 2 it is easy to observe that the SNAP predictions are within a deviation of 20 meV/atom from their corresponding DFT references for the lattice deformation region of -2.0% $\leq \Delta a \leq$ 2.0% and -6.0% $\leq \Delta c \leq$ 2.0%. A relatively larger deviation shows up only for rather severe deformations, namely Δa beyond $\pm$5.0%. Since ZrB_2 is an extremely stiff crystal (Young's modulus reported between 490 GPa and 526 GPa[26,27]) with relatively small thermal expansion (see the relevant region noted within the red box of Fig. 2), the feasible thermal deformation region is limited and is well covered within

TABLE II. Generation protocol for the DFT reference configurations. For each data class we list the number of inequivalent configurations computed, $N_{\rm conf}$, the total number of atoms included in the simulation cell, $N_{\rm atoms}$, and the range of volume expansion/compression, V/V_0, measured with respect to the $T = 0$ K equilibrium volume, V_0. The last column describes the procedure used to generate the specific dataset. The *EOS* (equation of state) class includes configurations obtained by altering the a and c lattice parameters separately, while keeping the atomic positions frozen at their equilibrium values. In the *Distorted* class atoms are randomly displaced from their equilibrium positions. The *MD snapshots* class includes configurations taken from molecular dynamics (MD) simulations in the NVT ensemble performed with the on-the-fly SNAP force field in the temperature range 100 K-1800 K. The *Deformed* class contains configurations obtained for supercells strained along one of the elementary deformation modes (see details in the SI), while the atomic positions are either from MD simulations or are obtained by random atomic displacement.

Data Class	$N_{\rm conf}$	$N_{\rm atoms}$	V/V_0 (%)	Generation scheme
EOS I	3	3	1.5 – 3.0	a and c are altered with the atoms kept at their equilibrium positions
Distorted I	309	81	0.0 – 3.7	The Zr and B atomic positions are randomly displaced from equilibrium with a maximum displacement of $d_{\rm max}$ = 0.01/0.05/0.08/0.10/0.15 Å
Distorted II	800	81	1.7 – 3.7	Only the B atomic positions are randomly displaced from equilibrium with a maximum displacement of $d_{\rm max}$ = 0.05/0.07/0.13/0.20 Å
MD snapshots I	338	81	0.6 – 2.0	MD snapshots collected every 0.1 ps from an NVT ensemble
Deformed I	400	81	1.4 – 4.0	The atomic positions are from MD snapshots (0.1 ps in the NVT ensemble), while the cell is strained by 1% along various deformation directions
MD snapshots II	1119	81	-1.3 – 4.1	MD snapshots collected every 0.1 ps from an NVT ensemble
Deformed II	120	108	1.0	The atomic positions are randomly displaced with $d_{\rm max}$ =0.10 Å, while the cell is strained by 1% along various deformation directions
Deformed III	513	81	-3 – 2.0	The atomic positions are randomly displaced with $d_{\rm max}$ =0.13 Å, while the cell is strained by 1% along various deformation directions
EOS II	242	3	-28.5 – 40.6	a and c are altered with the atoms kept at their equilibrium positions

the high-accuracy domain of SNAP force field.

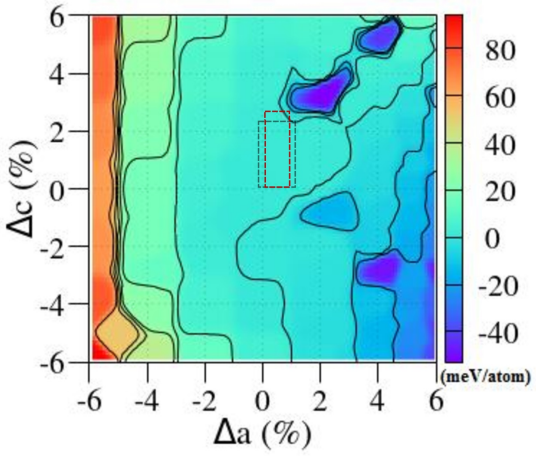

FIG. 2. (color online) Evaluation of the SNAP accuracy in computing the total energy as a function of the variation of the lattice parameters Δa and Δc (in %). The color scale indicates the RMS energy error (in meV/atom). The grey and red boxes show the relatively small region included in training process and the relevant thermal expansion domain upto 2500 K, respectively.

Finally, Fig. 3 illustrates the excellent performance of the SNAP force field in calculating the phonon bands as compared with the DFT results. In both cases the dynamical matrices are derived using the finite difference method, for which the $3 \times 3 \times 3$ supercells with finite atomic displacement of 0.01 Å are adopted. Then, a Fourier interpolation over a dense $108 \times 108 \times 108$ mesh, performed with the PHONOPY code[28,29], is used to obtain a smooth frequency dispersion. The good agreement of the phonon bands computed with SNAP and DFT in Fig. 3, indicates that our SNAP force field is not only capable of describing the potential energy surface, but also to qualitatively account for its derivatives.

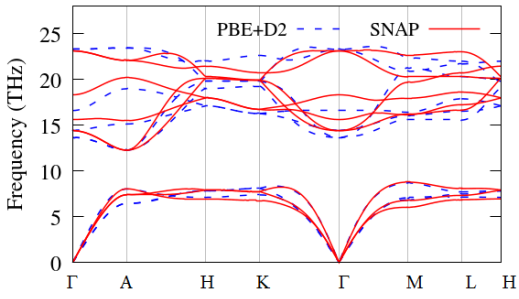

FIG. 3. (color online) Phonon dispersion curves calculated with SNAP (in red) and DFT PBE+D2 (in blue).

III. APPLICATIONS

In what follows we will evaluate the ability of our force field to predict several T-dependent fundamental physical properties of ZrB_2. We will begin with its performance around room temperature, then move to the high-temperature region. Finally we will discuss the challenges encountered at extremely high temperatures (above 2000 °C).

A. Room-temperature properties

We start our analysis by looking at the ZrB_2 structural and elastic properties near room temperature. In Table III we report the calculated values for the lattice

parameters, a and c, the elastic constants, c_{ij}, the bulk modulus, B, the Young's modulus, E, and the shear modulus, G. These are compared to the measured experimental values[26,27,30] and to our DFT PBE+D2 predictions. Furthermore, we include in the table the published data obtained with two different parameterizations of the Tersoff potential[14].

In general we find a rather good agreement over the entire range of properties between our SNAP predictions and the DFT target. Importantly, since DFT at the level of PBE+D2 provides an excellent description of the experimental data, such agreement with experiments is transferred to our SNAP force field. Going into more detail, we note that DFT[23] slightly underestimates the experimental lattice parameters[30], being $a = 3.162$ Å and $c = 3.493$ Å instead of $a = 3.170$ Å and $c = 3.532$ Å. SNAP, which is trained over DFT PBE+D2 data, as expected maintains such underestimation and returns us the lattice parameters $a = 3.164$ Å and $c = 3.486$ Å. Notably, SNAP outperforms the two available Tersoff models, which further overbind, in particular along the a axis (3.131 Å $< a <$ 3.140 Å).

Turning our attention to the elastic constants and moduli we remark again the good agreement between DFT and experiments [26,27] and the ability of SNAP to reproduce the DFT results, and hence the experimental ones. The only exception is for the c_{44} constant, that SNAP overestimates by about 25%. Such error propagates in the overestimation of both G and B. Note that we could have improved the SNAP description of the elastic properties by including in the training set additional configurations describing low temperature distortions. However, our objective is to obtain a potential performing over a wide temperature range, so that our training set needs to remain well balanced. As such, we effectively trade some accuracy in describing the room-temperature elastic tensor for a large dynamic range. Finally, as for the structural properties, also for the elastic ones SNAP outperforms completely the available Tersoff potentials[14], which in general are not capable to even rank the magnitude of the various elastic constants.

B. High-temperature properties

We now move to explore how our optimized SNAP force field is able to describe the various properties in a temperature range comprised between 300 K and 2500 K. Firstly, we investigate the thermal expansion effects by calculating the temperature-dependent lattice parameters, $a(T)$ and $c(T)$. This is performed by sampling the NPT molecular-dynamics trajectories over 100 ps for various temperatures. The SNAP potential predicts the thermal expansion along the c axis to be relatively higher than that along a, as shown in Fig. 4. Experimental data[26] are available up to 1,200 K, a temperature range described extremely well by our SNAP force field, which again traces well the DFT results obtained using the quasi-harmonic approximation of phonon calculations at the PBE+D2 level. The excellent agreement between SNAP and DFT, in fact, extends up to 2,000 K. Note the latter is a static calculation method, being computationally heavy and the anharmonic effects can only be suitable considered within finite temperatures, below 2000 K. Most importantly the SNAP predictions can reach 2,500 K, meaning that our atomic potential is capable to explore the ultra-high temperature region, where experiments are difficult to perform and are not yet available.

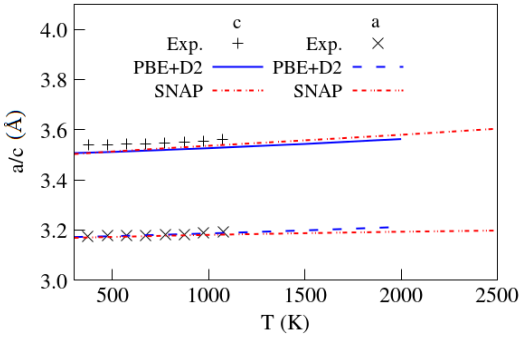

FIG. 4. (color online) Variation of the lattice parameters, a and c (in Å), with temperature. The SNAP results (in red) obtained from NPT molecular dynamics (averaged over 100 ps) are compared with the those from DFT PBE+D2 (in blue) and experiments[26] (in black).

We then move to determine the temperature dependence of the elastic tensor, c_{ij}, as computed from SNAP. This quantity is determined from the trajectories of NVE molecular dynamics simulations by using the explicit deformation method[31] (see computational details in the SI). During the simulations the lattice parameters as a function of temperature, $a(T)$ and $c(T)$, are fixed to those previously derived by SNAP and reported in Fig. 5.

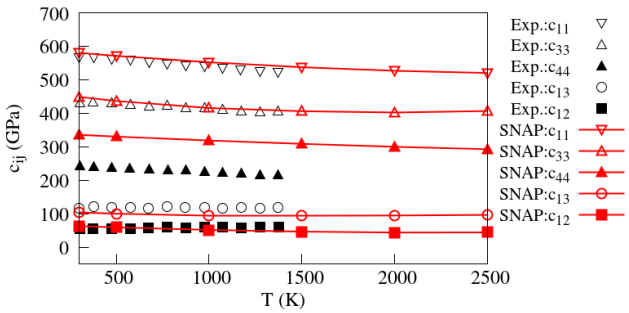

FIG. 5. (color online) Variation of the elastic constants, c_{ij} (GPa), with temperature. The SNAP results (in red) are extracted from the NVE trajectories over a 250 ps interval after an initial equilibration of 150 ps. Results are compared with available experiments[26] (in black).

The results of $c_{ij}(T)$ are presented in Fig. 5, where a good agreement with experiments[26] is achieved over the temperature range where experiments are available. The agreement is particularly good for the elastic tensor components c_{11}, c_{33}, c_{12} and c_{13}, while that for c_{44} is less satisfactory. Note that, in general, the deviation of c_{44} with respect to the experimental value at high temperature simply follows the same deviation found at room temperature (see Table III). It is important to point out that c_{44} is related to the elastic response of the cell to shear strains. Our training data set is dominated by configurations constructed over undistorted cells (1447), and only a small fraction contains biaxial deformed ones (403). In principle, further improvements in c_{44} can then

TABLE III. Room-temperature structural and elastic properties of ZrB_2 calculated with our SNAP force field. Results are compared to experiments, to DFT (PBE+D2) estimates and to predictions obtained with Tersoff potentials.[14]

	Exp.[26,27,30]	PBE+D2[23]	Tersoff$_{P1}$[14]	Tersoff$_{P2}$[14]	SNAP
a (Å)	3.170	3.162	3.140	3.131	3.163
c (Å)	3.532	3.493	3.547	3.484	3.486
c_{11} (GPa)	568	584	422	575	580
c_{33} (GPa)	441	431	320	817	449
c_{44} (GPa)	258	253	119	246	336
c_{12} (GPa)	57	56	156	213	63
c_{13} (GPa)	121	116	171	301	104
B (GPa)	224-240	251	240	400	238
G (GPa)	216-232	208	118	211	268
E (GPa)	490-526	488	–	–	586

be obtained by increasing the training set to add sheared configurations. This, however, should be done without unbalancing the training set, that otherwise will be unsuitable to capture the behaviour of the remaining c_{ij} constants. Considering the general good agreement of the overall elastic tensor this further refinement has not been performed.

Finally we turn our attention to the variation of the thermal conductivity with a wide range of temperatures, which is satisfactorily derived using our SNAP force field. In this case the lattice thermal conductivity tensor, κ_{ij}, is calculated by using the equilibrium Green-Kubo formalism[32]. In particular, κ_{ij} is evaluated from NVE molecular dynamics simulations of heat flux up to 40 ns, a time needed to achieve convergence at temperatures comprised between 300 K and 2500 K (see computational details in SI).

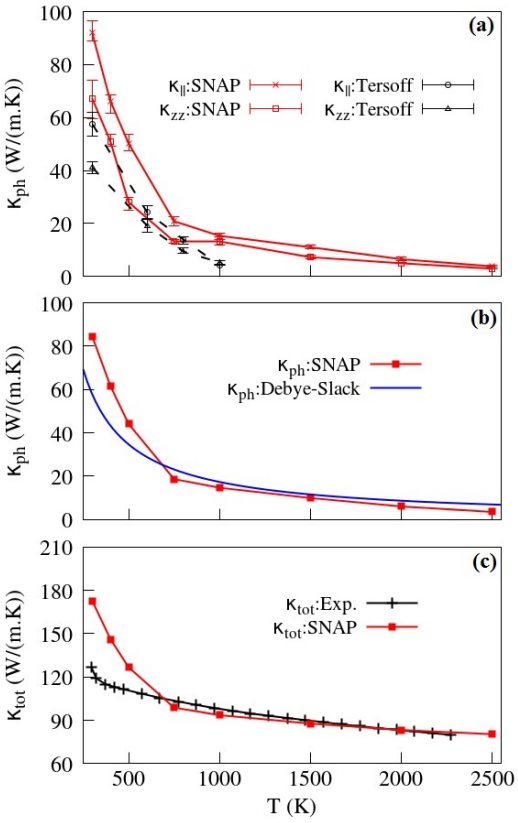

FIG. 6. (color online) Thermal conductivity, κ (in units of W/m·K), as a function of the temperature. In panel (a) the SNAP predictions (in red) for the in-plane, $\kappa_{||}$, and out-of-plane, κ_{zz}, components of the lattice thermal conductivity are compared with results obtained with a Tersoff potential (in black)[16]. Panel (b) shows the orientation-averaged lattice thermal conductivity computed with SNAP (in red) together with an estimate obtained from the Debye-Slack model (in blue). Panel (c) shows the the total calculated thermal conductivity, $\kappa_{\rm tot} = \kappa_{\rm ph} + \kappa_{\rm el}$ (red), in comparison with experiments (black)[26]. In this case the electronic thermal conductivity is estimated based on the Wiedmann-Franz law.

The calculated in-plane, $\kappa_{||}$, and out-of-plane, κ_{zz}, lattice thermal conductivities as a function of temperature are shown in Fig. 6(a). SNAP returns us an anisotropic lattice thermal conductivity for temperatures up to about 1,000 K, while it is essentially isotropic at elevated temperatures. The anisotropy remains, however, rather moderate even in the low temperature region. Available theoretical results obtained with a Tersoff force field are also

presented[16]. These are limited to temperatures up to 1,000 K and constantly return κ values smaller than those computed by SNAP, although also the Tersoff potential captures the anisotropy. It was argued in the past[16] that a phonon thermal conductivity of 5 W/m·K at 1000 K, as obtained with the Tersoff force field, is too low when compared to experiments. SNAP improves on such determination and predicts κ to be around 15 W/m·K at 1000 K. This improved consistency with experiments originates from the accurate description of the interatomic interaction offered by SNAP. Since the lattice thermal conductivity is dominated by phonon scattering processes, the accurate SNAP description of the forces makes it possible to accurate calculate the heat flux and thereby to successfully predict κ. This is true not only at relatively lower temperature, but over a wide temperature range extending up to ultra-high temperatures, as we will demonstrate in the following.

The lattice thermal conductivity at high temperatures can be estimated by using the Debye-Slack model[33,34]. In Fig. 6(b) we present the average lattice thermal conductivity, $\kappa_{\rm ph}$, in comparison with the Debye-Slack prediction (see details in SI). The $\kappa_{\rm ph}(T)$ curve is defined as the square average of the diagonal components of the conductivity tensor, $\kappa_{\rm ph} = 1/3\sqrt{\kappa_{11}^2 + \kappa_{22}^2 + \kappa_{33}^2}$. We find that above 1000 K, our SNAP results agree well with the $\kappa_{\rm ph}$ determined with the Debye-Slack model. At lower temperatures the agreement is less good with the SNAP predictions being constantly above the Debye-Slack curve. This is expected, since the Debye-Slack model is designed to estimate the thermal resistivity at temperatures above the Debye temperature, $\theta_{\rm D}$. In fact, it assumes Umklapp scattering to be the dominant process limiting the thermal conductivity and completely ignores contributions from scattering to the optical phonon branches. This kind of approximation works in the high temperature limit, but underestimates $\kappa_{\rm ph}$ for $T < \theta_{\rm D}$. In contrast, our SNAP force field provides a robust tool to perform molecular dynamic simulations of heat transfer over the full temperature spectrum. At the same time it bears a much higher accuracy and efficiency.

Finally in Fig. 6(c) we compare the total thermal conductivity, $\kappa_{\rm tot} = \kappa_{\rm ph} + \kappa_{\rm el}$, with experiments. Here the $\kappa_{\rm tot}(T)$ curve is obtained by adding to the SNAP-calculated lattice thermal conductivity, the electronic contribution, $\kappa_{\rm el}$. The latter is estimated by using the Wiedemann-Franz law with data for the temperature-dependent electrical conductivity taken from available experiments (see SI). Notably, our $\kappa_{\rm tot}$ is in excellent agreement with that measured in experiments[26] for all temperature above 600 K. Deviations at low temperature are possibly due to phonon scattering to crystal defects, grain boundaries and surfaces. These mechanisms, which in general reduce the lattice conductivity, are not included in our SNAP calculations. Note that reductions in the electrical conductivity due to defect scattering are already taken into account by the use of experimental data when determining $\kappa_{\rm el}$.

C. Challenges emerging at ultra-high temperatures

The SNAP force field that we have just presented (named 'SNAP-I') describes remarkably well several temperature-dependent physical properties of ZrB_2 up to 2500 K. At the same time 'SNAP-I' maintains the dynamical stability of ZrB_2 over all the temperatures investigated. The next question is how well can the SNAP force field simultaneously describe the dynamic stability of ZrB_2 above 2600 K and maintain high accuracy in determining the T-dependent physical properties. The construction of a force filed describing the ultra-high temperature region requires additional configurations to be included in the training set. These should explore geometries characterized by larger bond lengths and lattice distortions. We have performed such exercise and generated a full range of novel SNAP force fields.

Our results suggest that a SNAP force field able to retain the dynamic stability of ZrB_2 to temperatures up to 3,300 K and possibly above can be constructed. However, in the construction we have to relax its performance in predicting the elastic and mechanical properties at low temperature. In all cases, unfortunately, an extension of the dynamical range of the force field above 2,600 K always comes at the expenses of the accuracy in describing the mechanical properties below 2,000 K. In particular we were not able to match the description of the temperature dependent elastic tensor provided by 'SNAP-I'. In any case, the results for our best attempt, 'SNAP-II', are presented in Fig. 7 to demonstrate the feasibility of extending the dynamic stability.

In the Fig. 7, panel (a) and (b) present the mean squared displacements (MSDs) computed with SNAP-I and SNAP-II, respectively, over an NVT-ensemble trajectory of 1 ns. As expected the MSD of the lighter B atoms is consistently above that of Zr at any temperature, regardless of the SNAP version used. The MSD increases with temperature linearly below 1500 K, which is similar for the two force fields. However, at 2,600 K the MSDs calculated for SNAP-I suddenly take extremely large values, indicating that the force field is no longer able to capture the movement of certain atoms. In contrast, SNAP-II does not present such discontinuity in the MSDs, which retain a smooth dependence with the temperature. More significant thermal disturbance is observed for the B atoms at temperatures between 3,200 K and 3,300 K. It is, in fact, around these values that the MSD for B surpasses the boundary established by Lindermann's law for melting, i.e. $0.07 \times d_{\rm B-B} \sim 0.128$ Å, where $d_{\rm B-B}$ is the equilibrium B-B bond length. We then conclude that, in general, SNAP is capable of describing the dynamics at ultra-high temperatures, although with a compromise about its low temperature accuracy. Future work is needed to develop a consistently accurate force field capable to describe ZrB_2 up to the melting point.

IV. CONCLUSIONS

In this work we have developed a machine learned SNAP force field for ZrB_2, one important ultra-high temperature ceramic for the fabrication of the hot components in the aerospace and nuclear industries. After having detailed the procedure to construct a balanced training set, we have shown how such force field can describe the structural, mechanical, thermodynamics, and thermal transport properties, both at room and at high temperatures. In particular, it provides a reliable and efficient tool to compute the lattice thermal conductivity across a wide temperature range. Relying on the richness of its training dataset and the limited number of model

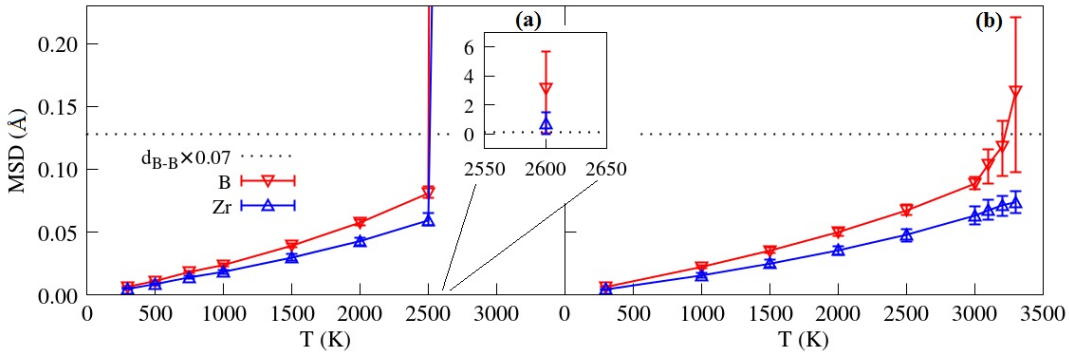

FIG. 7. (color online) Temperature-dependent mean-squared displacement (MSD, in Å) for Zr (in blue) and B (in red) atoms predicted using (a) 'SNAP-I' and (b) 'SNAP-II', respectively. The inset shows the behaviour of 'SNAP-I' at 2,600 K. The dashed horizontal line marks the boundary established by Lindermann's law for melting, MSD $> 0.07 \times d_{\mathrm{B-B}} \sim 0.128$ Å, with $d_{\mathrm{B-B}}$ being the B-B equilibrium bond length.

parameters our SNAP can successfully and efficiently capture the T-dependent properties from room temperature to 2500 K. This covers completely the temperature range required by applications, making our SNAP potential an important tool for exploring materials properties not easily accessible by experiments. Overall our work demonstrates the possibility to construct DFT-accurate force fields for materials operating in extreme conditions.

ACKNOWLEDGEMENT

We acknowledge G.C. Sosso (University of Warick) for the useful discussions. This work is supported by the European Union's Horizon 2020 "Research and innovation programme" under the grant agreement No.685594 (C^3HARME). Computational resources have been provided by the Irish Center for High-End Computing (ICHEC) and the Trinity Centre for High Performance Computing (TCHPC). The code for fitting the SNAP force field can be found at https://github.com/lunghiale/fitsnap.

REFERENCES

[1] Y. Z. William G. Fahrenholtz, Eric J. Wuchina, William E. Lee (Ed.), Ultra-High Temperature Ceramics Materials for Extreme Environment Applications, John Wiley & Sons, 2014.
[2] M. Caccia, M. Tabandeh-Khorshid, G. Itskos, A. R. Strayer, A. S. Caldwell, S. Pidaparti, S. Singnisai, A. D. Rohskopf, A. M. Schroeder, D. Jarrahbashi, T. Kang, S. Sahoo, N. R. Kadasala, A. Marquez-Rossy, M. H. Anderson, E. Lara-Curzio, D. Ranjan, A. Henry, K. H. Sandhage, Ceramicmetal composites for heat exchangers in concentrated solar power plants, Nature 562 (2018) 406–409.
[3] N. P. Padture, Advanced structural ceramics in aerospace propulsion, Nat. Mater. 15 (2016) 804–809.
[4] Y. Zeng, D. Wang, X. Xiong, X. Zhang, P. J. Withers, W. Sun, M. Smith, M. Bai, P. Xiao, Ablation-resistant carbide Zr0.8Ti0.2C0.74B0.26 for oxidizing environments up to 3,000C, Nat. Commun. 8 (2017) 15836.
[5] W. G. Fahrenholtz, G. E. Hilmas, Ultra-high temperature ceramics: Materials for extreme environments, Scr. Mater. 129 (2017) 94–99.
[6] T. Csanádi, J. Wehrs, S. Grasso, M. Reece, J. Michler, J. Dusza, Anomalous slip of ZrB2 ceramic grains during in-situ micropillar compression up to 500 C, Int. J. Refract. Met. Hard Mater. (2019).
[7] T. Ghidini, Materials for space exploration and settlement, Nat. Mater. 17 (2018) 846–850.
[8] A. Lunghi, S. Sanvito, A unified picture of the covalent bond within quantum-accurate force fields : From organic molecules to metallic complexes ' reactivity, Sci. Adv. 5 (2019) eaaw2210.
[9] G. C. Sosso, V. L. Deringer, S. R. Elliott, G. Csányi, Understanding the thermal properties of amorphous solids using machine-learning-based interatomic potentials, Mol. Simul. 44 (2018) 866–880.
[10] N. Artrith, A. Urban, G. Ceder, Efficient and accurate machine-learning interpolation of atomic energies in compositions with many species, Phys. Rev. B 96 (2017) 1–5.
[11] S. Rostami, M. Amsler, S. A. Ghasemi, Optimized symmetry functions for machine-learning interatomic potentials of multi-component systems, J. Chem. Phys. 149 (2018) 124106.
[12] A. P. Thompson, L. P. Swiler, C. R. Trott, S. M. Foiles, G. J. Tucker, Spectral neighbor analysis method for automated generation of quantum-accurate interatomic potentials, J. Comput. Phys. 285 (2015) 316–330.
[13] P. Vajeeston, P. Ravindran, C. Ravi, R. Asokamani1, Electronic structure, bonding, and ground-state properties of Al2-type transition-metal diborides, Phys. Rev. B 63 (2001) 45115.
[14] M. S. Daw, J. W. Lawson, C. W. Bauschlicher Jr, Interatomic potentials for Zirconium Diboride and Hafnium Diboride, Comput. Mater. Sci. 50 (2011) 2828–2835.
[15] A. Gouissem, W. Fan, A. C. T. Van Duin, P. Sharma, A reactive force-field for Zirconium and Hafnium Di-Boride, Comput. Mater. Sci. 70 (2013) 171–177.
[16] J. W. Lawson, M. S. Daw, C. W. Bauschlicher, Lattice thermal conductivity of ultra high temperature ceramics ZrB2 and HfB2 from atomistic simulations, J. Appl. Phys. 110 (2011) 83507.
[17] J. F. Ziegler, J. P. Biersack, The Stopping and Range of Ions in Matter, Springer US, Boston, MA, 1985, pp. 93–129. URL: https://doi.org/10.1007/978-1-4615-8103-1{_}3. doi:doi:10.1007/978-1-4615-8103-1˙3.
[18] A. P. Bartok, M. C. Payne, R. Kondor, G. Csanyi, Gaussian approximation potentials: The accuracy of quantum mechanics, without the electrons, Phys. Rev. Lett. 104 (2010) 1–4.
[19] P. E. Blöchl, Projector augmented-wave method, Phys. Rev. B 50 (1994) 17953–17979.
[20] G. Kresse, D. Joubert, From ultrasoft pseudopotentials to the projector augmented-wave method, Phys. Rev. B 59 (1999) 1758–1775.
[21] J. P. Perdew, K. Burke, M. Ernzerhof, Generalized gradient approximation made simple, Phys. Rev. Lett. 77 (1996) 3865–3868.
[22] S. Grimme., Semiempirical GGA-type density functional constructed with a long-range dispersion correction, J. Comput. Chem. 27 (2006) 1787–1799.
[23] Y. Zhang, S. Sanvito, First-principles investigation of the thermodynamic stability of MB2 materials surfaces (M = Ti / Zr / Hf), J. Am. Ceram. Soc. 101 (2018) 4118–4127.
[24] S. Plimpton, Fast Parallel Algorithms for Short-Range Molecular Dynamics, J. Comput. Phys. 117 (1995) 1–19.
[25] P. Rowe, G. Csányi, D. Alfè, A. Michaelides, Development of a machine learning potential for graphene, Phys. Rev. B 97 (2018) 1–12.
[26] N. L. Okamoto, M. Kusakari, K. Tanaka, H. Inui, S. Otani, Anisotropic elastic constants and thermal expansivities in

monocrystal CrB2, TiB2, and ZrB2, Acta Mater. 58 (2010) 76–84.
[27] F. Nakamori, Y. Ohishi, H. Muta, K. Kurosaki, K. I. Fukumoto, S. Yamanaka, Mechanical and thermal properties of bulk ZrB2, J. Nucl. Mater. 467 (2015) 612–617.
[28] A. Togo, Phonopy, 2017. URL: https://atztogo.github.io/phonopy/.
[29] A. Togo, I. Tanaka, First principles phonon calculations in materials science, Scr. Mater. 108 (2015) 1–5.
[30] V. A. Gasparov, N. S. Sidorov, I. I. Zver'kova, M. P. Kulakov, Electron transport in diborides: Observation of superconductivity in ZrB2, J. Exp. Theor. Phys. Lett. 73 (2001) 532–535.
[31] G. Clavier, N. Desbiens, E. Bourasseau, V. Lachet, N. Brusselle-Dupend, B. Rousseau, Computation of elastic constants of solids using molecular simulation: comparison of constant volume and constant pressure ensemble methods, Mol. Simul. 43 (2017) 1413–1422.
[32] R. Zwanzig, Time-Correlation Functions and Transport Coefficients in Statistical Mechanics, Annu. Rev. Phys. Chem. 16 (1965) 67–102.
[33] D. Morelli, G. Slack, High Lattice Thermal Conductivity Solids, in: S. Shindé, J. Goela (Eds.), High Therm. Conduct. Mater., Springer New York, 2006, pp. 37–68. URL: http://dx.doi.org/10.1007/0-387-25100-6{_}2. doi:doi:10.1007/0-387-25100-6˙2.
[34] Y. Zhang, B. Liu, J. Wang, J. Wang, Theoretical investigations of the effects of ordered carbon vacancies in ZrC1-x on phase stability and thermo-mechanical properties, Acta Mater. 111 (2016) 232–241.